Nonlinear generation of vector beams by using a compact nonlinear fork grating

Qian Yang,[1,†] Yangfeifei Yang,[1,†] Hao Li,[1] Haigang Liu,[1,3] and Xianfeng Chen[1,2,4]

[1]*State Key Laboratory of Advanced Optical Communication Systems and Networks, School of Physics and Astronomy, Shanghai Jiao Tong University, Shanghai 200240, China*
[2]*Shanghai Research Center for Quantum Sciences, Shanghai 201315, China*
[3]*e-mail: liuhaigang@sjtu.edu.cn*
[4]*e-mail: xfchen@sjtu.edu.cn*
[†]*These authors contributed equally to this work.*

Vectorial beams have attracted great interest due to their broad applications in optical micromanipulation, optical imaging, optical micromachining, and optical communication. Nonlinear frequency conversion is an effective technique to expand the frequency range of the vectorial beams. However, the scheme of existing methods to generate vector beams of the second harmonic (SH) lacks compactness in the experiment. Here, we introduce a new way to realize the generation of vector beams of SH by using a nonlinear fork grating to solve such a problem. We examine the properties of generated SH vector beams by using Stokes parameters, which agree well with theoretical predictions. Then we demonstrate that linearly polarized vector beams with arbitrary topological charge can be achieved by adjusting the optical axis direction of the half-wave plate (HWP). Finally, we measure the nonlinear conversion efficiency of such a method. The proposed method provides a new way to generate vector beams of SH by using a microstructure of nonlinear crystal, which may also be applied in other nonlinear processes and promote all-optical waveband applications of such vector beams. © 2024 Chinese Laser Press

1. INTRODUCTION

Since the vectorial optical fields were first carried out by Snitzer in 1961 [1], there has been an increasing attention in vector beams due to their special spatially inhomogeneous polarization states across the transverse section of the beams. The generation of such vector beams can be classified into active and passive methods. Grating mirrors or Brewster prisms [2,3] can be used to select the desired polarization mode in intra-cavity, which is the active method. The passive methods are based on the polarization reconstruction of traditional laser with the aid of spatial light modulators (SLMs) [4], q-plates [5], and meta-surfaces [6]. The distinctive polarization distribution of vector beams results in unique properties when they interact with matter and offers advantages in lots of fields. Radially polarized vector beams can be focused into a tighter spot than that of spatially homogeneous polarization beams and form a strong and localized longitudinal component [7], which can be widely used in optical trapping [8,9], high-accuracy laser microma-chining [10,11], and optical super-resolution imaging [12]. The special polarization of such vector beams can excite plas-monic beams with special polarization [13]. The high dimen-sionality of vector beams enhances channel capacity, which can

be applied in classical and quantum communication. Vector beams suffer less from turbulent atmosphere than Gaussian beams [14], which are suitable for long-range optical communications in complex environments [15].

With the continued development of laser applications, there has been a growing need for a diversity of laser wavelengths. Nonlinear frequency conversion is an effective method to extend the range of obtainable wavelengths from existing laser sources. Therefore, nonlinear frequency conversion of vector beams has been proposed in recent years. Nonlinear frequency conversion of vector beams by using two cascading orthogonally placed nonlinear crystals in the three-wave mixing process was demonstrated in 2018 [16]. Nonlinear generation of ultra-fast and high-order vector vortex beams through a single-pass second-harmonic generation (SHG) process has also been demonstrated by using such a dual crystal scheme [17]. Then, SHG [18] and third-harmonic generation (THG) [19] of vector beams in a Sagnac loop have been demonstrated. In addition, nonlinear generation of vector beams can also be achieved by using a Mach–Zehnder interferometer [20]. Afterwards, a dual-waveband generator is proposed to simultaneously generate perfect vector beams in linear and nonlinear wavebands

[21]. Nonlinear generation of ultraviolet vector beams [22] and perfect vector beams [23] has also been studied. In addition, some studies focus on the vectorial feature of Poincaré beams during the SHG process from infrared waveband to visible full Poincaré beams [24,25]. And a technique to control the coverage of full Poincaré beams through SHG has been discussed [26]. In recent years, stimulated parametric down-conversion [27], parametric up-conversion [28], and conformal frequency conversion [29] processes of such vectorial structured light have also been studied theoretically and experimentally. However, all these methods are conducted in two steps to obtain vector beams of SH: the first step is to generate the vectorial optical fields by using the linear optical method, and the second step is to perform nonlinear transformation processes. Therefore, simplifying the experiment setup with microstructures is highly desired for the generation of vector beams of the SH.

In this paper, we demonstrate a new and compact method to generate nonlinear vectorial beams by using a microstructure, which etches a nonlinear fork grating on the surface of lithium niobate (LN) crystal. First of all, we verify the generation of SH vector beams with different topological charges theoretically and experimentally. Then we measure the polarization properties of the generated SH vector beams by using Stokes parameters, which are in accordance with the theoretical results. And we demonstrate the flexibility of this approach by rotating the axis direction of the half-wave plate (HWP) to change the polarization distributions of generated SH vector beams. Furthermore, we measure the nonlinear frequency conversion efficiency during this nonlinear process.

2. EXPERIMENT SETUP

The experimental setup is illustrated in Fig. 1. A high-energy diode-pumped all-solid-state Q-switched linearly polarized laser with the wavelength of 1064 nm, the repetition frequency

of 1 kHz, and the pulse duration of 10 ns is used as the light source. A half-wave plate (HWP_1) is used to adjust the polarization of the laser, and a Glan–Taylor (GT) prism is used to control the polarization states to obtain horizontally polarized light $\begin{pmatrix} 1 \\ 0 \end{pmatrix}$. And we can control the intensity of beams by adjusting the angle of the HWP_1. After that, HWP_2 is used to control the polarization states of generated SH vector beams and a $-45°$ quarter-wave plate (QWP_1) is used to make the beams propagating clockwise and anticlockwise in a Sagnac loop have the same intensity, which can be calculated as

$$E(\omega) = Q(-45°)H(\alpha)\begin{pmatrix} 1 \\ 0 \end{pmatrix} = \frac{1}{\sqrt{2}}\begin{pmatrix} e^{i2\alpha} \\ ie^{-i2\alpha} \end{pmatrix}, \quad \textbf{(1)}$$

where $E(\omega)$ represents the electric field of the fundamental frequency (FF) wave. $H(\alpha) = \begin{pmatrix} \cos 2\alpha & \sin 2\alpha \\ \sin 2\alpha & -\cos 2\alpha \end{pmatrix}$ and $Q(-45°) = \frac{1}{\sqrt{2}}\begin{pmatrix} 1 & i \\ i & 1 \end{pmatrix}$ denote the Jones matrices of the HWP_2 and QWP_1, respectively. α is the angle between the fast axis of the HWP_2 and horizontal direction. Three mirrors (M_1, M_2, and M_3) and the PBS compose a Sagnac loop. The FF beam is split into two parts with orthogonal polarization directions by using a PBS. In the Sagnac loop, the two separated counterpropagating FF beams propagate through the nonlinear fork grating, respectively. To ensure the spatial propagation and evolution of the two counterpropagating beams are the same, we place the nonlinear fork grating at the center of the Sagnac loop. Such a nonlinear fork grating is made by the ultraviolet photolithography assisted inductively coupled plasma (ICP) etching method on 0.5 mm thick LN crystal [30]. The cutting angle between the propagation direction and optical axis of the LN crystal is 75° to satisfy the Type I (o + o → e) phase-matching condition in our experiment. The size of the nonlinear fork grating is 1 mm × 1 mm, and the period is 50 μm. The
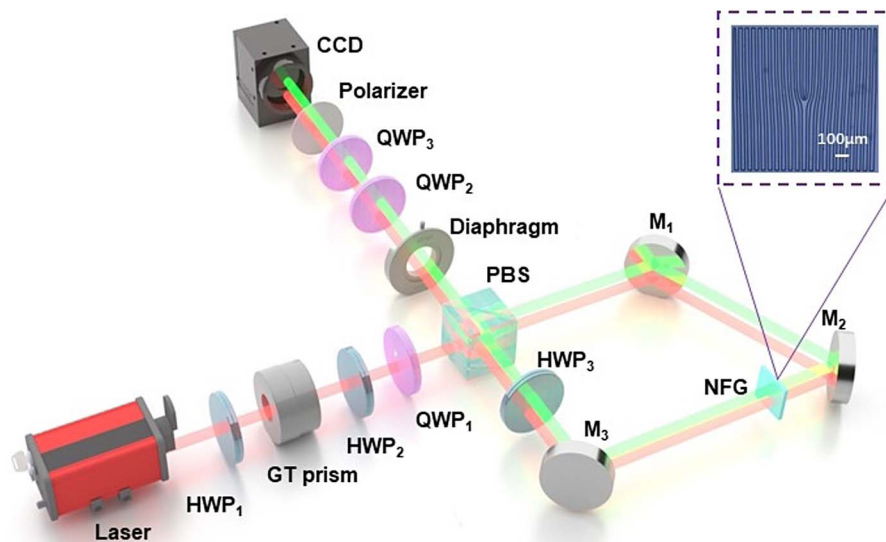

Fig. 1. Schematic of the experimental setup. GT prism, Glan–Taylor prism; HWP_1, HWP_2, and HWP_3, half-wave plates; QWP_1, QWP_2, and QWP_3, quarter-wave plates; PBS, polarized beam splitter; NFG, nonlinear fork grating; M_1, M_2, and M_3, mirrors; CCD, charge-coupled device. Inset shows the microscope image of fork grating etched on the LN surface.

structure of such a nonlinear fork grating with topological charge $\ell = 2$ is shown in the inset of Fig. 1. A dichroic HWP_3 is placed in the Sagnac loop to convert polarization directions. After the PBS, the o-polarized FF beam propagating clockwise satisfies the o + o → e phase-matching condition in the nonlinear frequency conversion process to generate an e-polarized SH beam, which is transformed into an o-polarized SH beam after the HWP_3. Another e-polarized FF beam in the Sagnac loop propagating anticlockwise is transformed into an o-polarized FF beam through the HWP_3 to achieve o + o → e nonlinear process. As a consequence, two SH beams with orthogonal polarizations can be recombined at the PBS. The nonlinear fork-shaped grating can produce nonlinear vortex beams with different topological charges along different diffraction directions. Specifically, the beam propagating clockwise first passes through the fork grating, and then through the nonlinear crystal. The topological charge of the generated SH vortex beams $\ell_{SH} = u\ell$, where u is the diffraction order of the generated SH vortex beam and ℓ is the topological charge of the nonlinear fork grating [31]. In our experiment, we used the positive first-order diffracted vortex beams. The evolution of the SH vortex beam can be expressed as

$$E_1'(2\omega) = \frac{i\omega d_{eff}}{cn_{2\omega}} A_1^2 L_0 b_1 \; \exp[i\vec{k}_{2t} \cdot \vec{r}$$
$$- i2\pi f(\vec{r}, \phi)] \exp(i\ell\phi), \quad (2)$$

where ω is the angular frequency of FF light, d_{eff} is the effective nonlinear coefficient, c is the light speed in vacuum, $n_{2\omega}$ is the refractive index of the SH beam, A_1 is the amplitude of the FF wave after separating by the PBS, $b_1 = \sum_{m,n}^{m+n=1} C_m C_n$ is the Fourier coefficient, $C_0 = \frac{1+e^{i\phi}}{2}$, $C_{m,n\neq0} = \frac{i[\cos(m\pi)-1]}{2m\pi}(1 - e^{i\phi})$, $\vec{k}_{2t}$ is the transverse wave vector, $\vec{r} = x\vec{x} + y\vec{y}$, ϕ is the azimuthal angle, $f(\vec{r}, \phi) = |\vec{r}| \cos(\phi)/\Lambda$ is the spiral structure function, Λ is the period parameter of the nonlinear fork grating, and L_0 is the length of the nonlinear crystal along the propagation direction. For the beam propagating anticlockwise, it first undergoes a nonlinear frequency conversion, and then the SH beam propagates through the linear fork grating. Accordingly, the generated negative first-order diffracted SH vortex beam can be written as

$$E_2'(2\omega) = \frac{i\omega d_{eff}}{cn_{2\omega}} A_1^2 L_0 C_{-1} \; \exp[i\vec{k}_{2t}' \cdot \vec{r}$$
$$+ i2\pi f(\vec{r}, \phi)] \exp(-i\ell\phi). \quad (3)$$

Therefore, after passing through the fork-shaped grating, the Jones matrices of beams propagating in opposite directions can be expressed as

$$E_1''(2\omega) = M_1 \begin{pmatrix} 0 \\ e^{i(\ell\phi+2\alpha)} \end{pmatrix},$$
$$E_2''(2\omega) = M_2 \begin{pmatrix} 0 \\ -ie^{-i(\ell\phi+\Delta_1+2\alpha)} \end{pmatrix}, \quad (4)$$

where $M_1 = -\frac{i\omega d_{eff}}{\sqrt{2}cn_{2\omega}} A_1^2 L_0 b_1 \; \exp[i\vec{k}_{2t} \cdot \vec{r} - i2\pi f(\vec{r}, \phi)]$, $M_2 = -\frac{i\omega d_{eff}}{\sqrt{2}cn_{2\omega}} A_1^2 L_0 C_{-1} \exp[i\vec{k}_{2t}' \cdot \vec{r} + i2\pi f(\vec{r}, \phi)]$. The exponential

terms satisfy the relation $\exp[i\vec{k}_{2t} \cdot \vec{r} - i2\pi f(\vec{r}, \phi)] = 1$ in M_1 and $\exp[i\vec{k}_{2t}' \cdot \vec{r} + i2\pi f(\vec{r}, \phi)] = 1$ in M_2 when we choose a particular diffraction order. Δ_1 represents the phase difference in the Sagnac loop which is caused by the birefringence of the PBS and nonlinear crystal [5% (molar fraction) MgO: $LiNbO_3$], and the optical path difference. Consequently, the two optical fields after the Sagnac loop can be written, respectively, in the form of

$$E_1'''(2\omega) = H(45°)E_{refl}E_{refl}E_1''(2\omega) = M_1 \begin{pmatrix} e^{i(\ell\phi+2\alpha)} \\ 0 \end{pmatrix},$$

$$E_2'''(2\omega) = E_{refl}E_{refl}E_2''(2\omega) = M_2 \begin{pmatrix} 0 \\ -ie^{-i(\ell\phi+\Delta_1+2\alpha)} \end{pmatrix}, \quad (5)$$

where $E_{refl} = \begin{pmatrix} -1 & 0 \\ 0 & 1 \end{pmatrix}$ represents the Jones matrix of mirrors. We would like to point out that the intensities of the generated SH beams propagating clockwise and anticlockwise are slightly different. We can adjust the axis direction of the QWP_1 to compensate the difference to make $M_1 = M_2 = M^T$. The two SH beams with orthogonal polarizations are recombined at the PBS. Therefore, the total optical field can be described as $E^T(2\omega) = E_1'''(2\omega) + E_2'''(2\omega) = M^T \begin{pmatrix} e^{i(\ell\phi+2\alpha)} \\ -ie^{-i(\ell\phi+\Delta_1+2\alpha)} \end{pmatrix}$.

After passing through the aperture diaphragm, two overlapping diffracted beams with opposite orders and topological charges are picked out. Then, the QWP_2 with a fast axis along 45° is employed to convert the two linearly polarized beams into vector beams. The Jones matrix of the generated SH vector beams can be derived as

$$E(2\omega) = Q(45°)E^T(2\omega)$$
$$= \sqrt{2}M^T e^{-i\left(\frac{\Delta_1}{2}-\frac{\pi}{2}\right)} \begin{pmatrix} \cos\left(l\phi + 2\alpha + \frac{\Delta_1}{2} - \frac{\pi}{2}\right) \\ \sin\left(l\phi + 2\alpha + \frac{\Delta_1}{2} - \frac{\pi}{2}\right) \end{pmatrix}. \quad (6)$$

Therefore, we can generate vector beams of SH with arbitrary topological charge. And we can generate vector beams with arbitrary polarization states by controlling the microstructure and the angle of the HWP_2 in theory. We would like to point out that we assume the angle of the QWP_1 is –45° when the angle of HWP_2 (α) is 0° in our theoretical analysis. In fact, when rotating the angle of the HWP_2, the angle of QWP_1 is changed accordingly to make the beams propagating clockwise and anticlockwise in the Sagnac loop have the same intensity in the experiment. Finally, our generated vector beams of SH are recorded by a charge-coupled device (CCD) shown in Fig. 1. A QWP_3 and a polarizer are used to analyze the polarization distributions of generated vector beams of SH.

3. EXPERIMENTAL RESULTS AND DISCUSSION

We rotate the angle α of the HWP_2 to set $2\alpha + \frac{\Delta_1}{2} - \frac{\pi}{2} = 0$; thus, Eq. (6) can be described as $E(2\omega) = \sqrt{2}M^T e^{-i(\frac{\Delta_1}{2}-\frac{\pi}{2})} \begin{pmatrix} \cos(l\phi) \\ \sin(l\phi) \end{pmatrix}$. For simplicity and without loss of generality, we generate SH vector optical fields with topological charges $\ell = 1, 2, 3$. The polarization distribution

can be characterized via measuring the Stokes parameters. To illustrate the Stokes parameters, we insert a QWP_3 and a polarizer before the CCD. The theoretical simulation and experimental results of Stokes parameters S_0, S_1, S_2, and S_3 of the generated SH vector beams are shown in Fig. 2. Figures 2(a1)–2(a4), 2(c1)–2(c4), and 2(e1)–2(e4) are theoretical simulations, and Figs. 2(b1)–2(b4), 2(d1)–2(d4), and 2(f1)–2(f4) show the corresponding experiment results. The first row of Fig. 2 refers to S_0 of the Stokes parameters, which represents the total intensity of SH vector beams. There is a polarization singularity at the center of the nonlinear vector beam. In addition, we can obviously see that the radius of the hollow spots increases with the topological charge increasing. As we know, positive S_1, S_2, and S_3 represent the components of linearly polarized beams polarized along the horizontal direction, linearly polarized beams along +45° with respect to the positive horizontal direction, and right-handed circularly polarized beams. Negative values of Stokes parameters describe the orthogonal polarization components. As shown in the second and third rows in Fig. 2, the beams are split into 4ℓ lobes. For the SH vector beams of $\ell = 1$, the positive and negative polarization directions of S_1 distribute along the horizontal and vertical directions, which can be seen in Figs. 2(a2) and 2(b2). In addition, the positive and negative polarization directions of S_2 are along +45° and –45° from the positive horizontal direction, which can be seen in Figs. 2(a3) and 2(b3). As for the situation $\ell = 2$ and 3, from Figs. 2(c2), 2(d2), 2(e2), and 2(f2), we find that the positive polarization directions of S_1 distribute along 0°, +90° and 0°, +60°, +120° with respect to the positive horizontal direction. And we see that negative polarization directions of S_1 appear when the positive polarization directions of S_1 rotate 45° and 30° with $\ell = 2$ and 3.

The components polarized along the positive polarization direction of S_2 are distributed at an angle of 45°, 22.5°, 15° relative to the positive polarization direction of S_1 for $\ell = 1, 2, 3$. From the fourth row of Fig. 2, we observe that the generated SH vector beams almost do not have circularly polarized components. Thus, experimental results are consistent with theoretical ones, and the Stokes parameters distributions reveal the vectorial property of the generated SH vector beams.

To verify the flexibility of the proposed method in generating vector beams of SH with different polarization states, we demonstrate two situations by rotating the axis direction of the HWP_2 (α) to set $2\alpha + \frac{\Delta_1}{2} - \frac{\pi}{2} = \frac{\pi}{3}$ and $2\alpha + \frac{\Delta_1}{2} - \frac{\pi}{2} = \frac{\pi}{2}$. And the corresponding generated SH vector beams can be described as $E'(2\omega) = \sqrt{2}M^T e^{-i(\frac{\Delta_1}{2} - \frac{\pi}{2})} \begin{pmatrix} \cos(l\phi + \frac{\pi}{3}) \\ \sin(l\phi + \frac{\pi}{3}) \end{pmatrix}$ and $E''(2\omega) = \sqrt{2}M^T e^{-i(\frac{\Delta_1}{2} - \frac{\pi}{2})} \begin{pmatrix} \cos(l\phi + \frac{\pi}{2}) \\ \sin(l\phi + \frac{\pi}{2}) \end{pmatrix}$, respectively. Figures 3 and 4, respectively, show the theoretical and experimental results of the intensity and polarization distributions. To check the polarization distribution, we placed a polarizer to perform projection measurements for SH vector beams. Polarization directions of the polarizer are, respectively, along 0°, 30°, 60°, 90°, 120°, and 150° with respect to the positive horizontal direction. The arrows represent the polarization direction of the polarizer. And the components polarized in the same direction as that of the polarizer can be recorded, while the orthogonal polarization is extinguished. From Figs. 3 and 4, the vector beams are split into 2ℓ fan-shaped patterns after passing through a polarizer. It is clear that the fan-shaped patterns are completely different when the axis direction of the HWP_2 varies. For the situation $2\alpha + \frac{\Delta_1}{2} - \frac{\pi}{2} = \frac{\pi}{2}$ with $\ell = 1$, the azimuthally
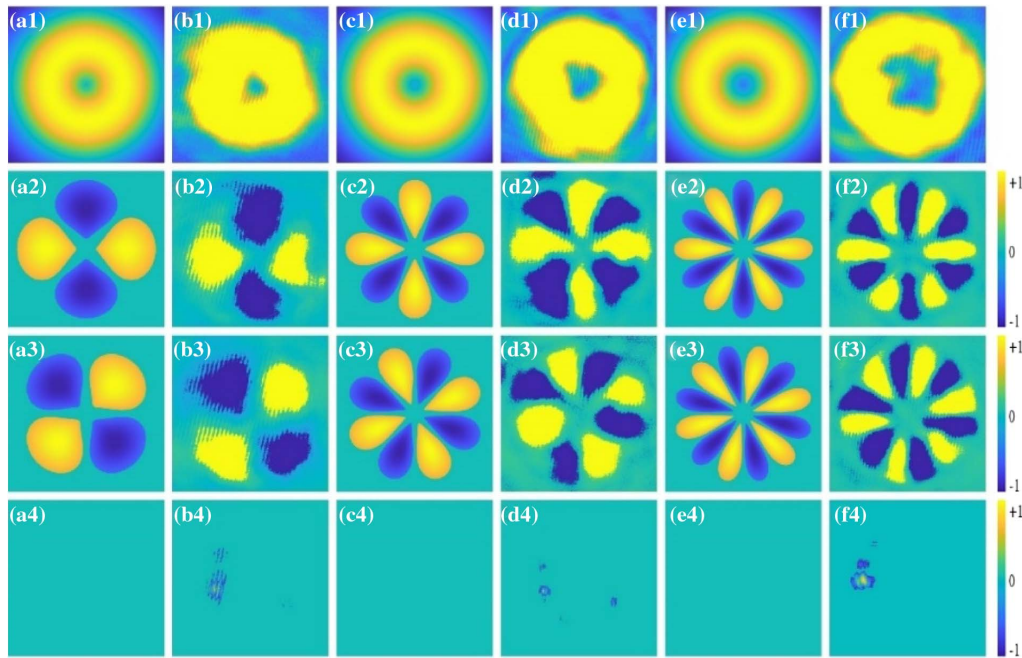

Fig. 2. Stokes parameters of SH vectorial light field. (a1)–(a4), (c1)–(c4), and (e1)–(e4), respectively, represent the simulated Stokes parameters S_0, S_1, S_2, and S_3 with the topological charge of $\ell = 1, 2, 3$. The corresponding experimental results are shown in (b1)–(b4), (d1)–(d4), and (f1)–(f4).
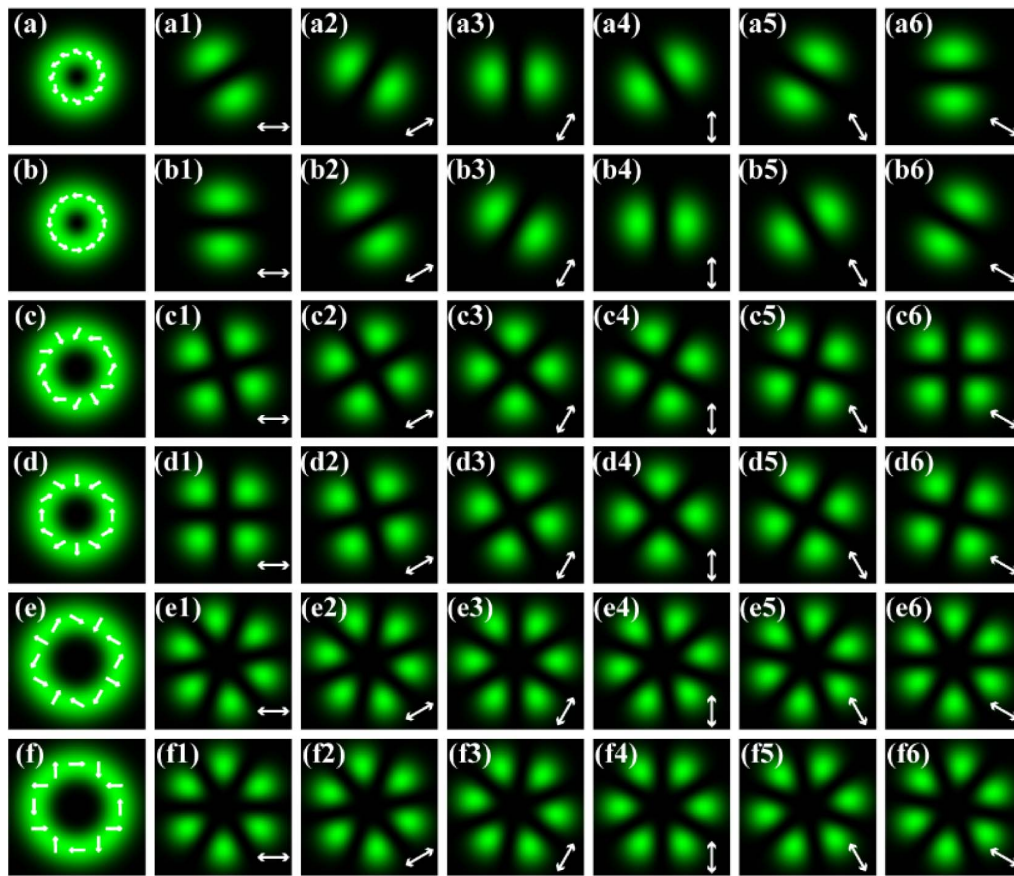
Fig. 3. First, third, fifth rows and second, fourth, sixth rows, respectively, show the results of the SH vector beams with the topological charge $\ell = 1, 2, 3$ when $2\alpha + \frac{\Delta_1}{2} - \frac{\pi}{2} = \frac{\pi}{3}$ and $2\alpha + \frac{\Delta_1}{2} - \frac{\pi}{2} = \frac{\pi}{2}$. Results from the second to seventh columns are intensity profiles of the generated vector beams when the polarizer has different polarization angles (0°, 30°, 60°, 90°, 120°, 150°) with respect to the positive horizontal direction. The corresponding simulated polarization distributions are displayed in (a)–(f). The arrows indicate the polarization direction of the polarizer.

polarized nonlinear vector beam is displayed, as shown in Fig. 3(b). The direction of the fan-shaped patterns rotates along the perpendicular direction with the orientation of the polarizer, as illustrated in Figs. 3(b1)–3(b6) and Figs. 4(b1)–4(b6). In the case of $2\alpha + \frac{\Delta_1}{2} - \frac{\pi}{2} = \frac{\pi}{3}$ with $\ell = 2$, when the polarizer has a polarization direction along the horizontal direction, the maximum intensity distributes at an angle of $+60°$, $+150°$ from the positive horizontal direction, which can be apparently seen in Figs. 3(c1) and 4(c1). And when the polarizer rotates from 0° to 90°, the four fan-shaped patterns gradually rotate 45°, as shown in Figs. 3(c1)–3(c4) and Figs. 4(c1)–4(c4). Also, the fan-shaped patterns as well rotate to the direction perpendicular to the original polarization distribution as the angle of the polarizer increases to 180°, as shown in Figs. 3 (c4)–3(c6) and Figs. 4(c4)–4(c6). From Figs. 3(e1)–3(e6) and Figs. 4(e1)–4(e6), we easily know that when $2\alpha + \frac{\Delta_1}{2} - \frac{\pi}{2} = \frac{\pi}{3}$ and $\ell = 3$, the horizontal polarization lobes distribute at an angle of $+40°$, $+100°$, $+160°$ with positive horizontal direction, and the six fan-shaped patterns rotate anticlockwise by 60° as the polarizer gradually rotates from 0° to 180°. However, for the situation of $2\alpha + \frac{\Delta_1}{2} - \frac{\pi}{2} = \frac{\pi}{3}$, the fan-shaped patterns almost appear at $+30°$, $+15°$, $+10°$ relative to the polarization distributions of $2\alpha + \frac{\Delta_1}{2} - \frac{\pi}{2} = \frac{\pi}{2}$ with $\ell = 1$,

2, 3. From Fig. 4, we can see that after passing through the polarizer, the polarization and intensity distributions of experimental results are in good agreement with the theoretical simulations. As shown in the first column of Fig. 4, the generated SH vector beams are not perfect doughnut intensity profiles, which may be caused by design precision and fabrication errors of the microstructures. The defects of the cross section of the structure affect the diffraction quality of the grating, and then affect the quality of generating SH vector beams. The vectorial properties of the generated SH vector beams are changed by simply rotating the axis direction of the HWP_2, and we can achieve vector beams of SH with arbitrary polarization in this way.

Moreover, we also measure the nonlinear frequency conversion efficiency of our method of generating SH vector beams. Figure 5 indicates the generated SH vector beams power (P_2) varies as the incident FF beams power (P_1) increases before the Sagnac loop. In the experiment, powers of two FF beams separated by the PBS are $\frac{P_1}{2} = \frac{1}{2} n_\omega \varepsilon_0 c |A_1|^2 S_{\text{eff}}$. n_ω and $n_{2\omega}$ are the refractive indices of the FF beams and SH beams, ε_0 is the vacuum permittivity, c is the speed of light in vacuum, and S_{eff} is the effective interaction area. After nonlinear processes, the powers of the two SH vortex beams propagating in opposite directions in the Sagnac loop are $P_2' = \frac{1}{2} n_{2\omega} \varepsilon_0 c |M^T|^2 S_{\text{eff}}$.
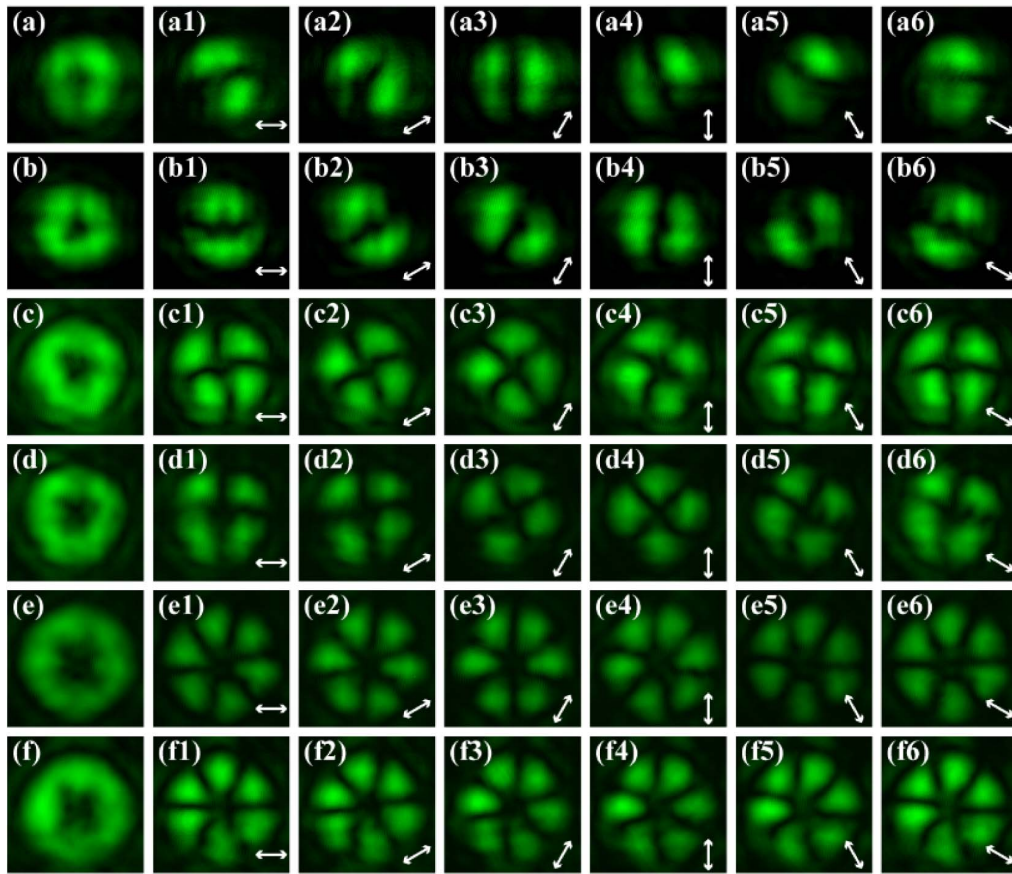
Fig. 4. Experimental results corresponding to the cases of Fig. 3. The arrows indicate the polarization direction of the polarizer.

Therefore, the total power of the generated SH vector beam can be expressed as $P_2 = \frac{1}{2} n_{2\omega} \varepsilon_0 c |\sqrt{2} M^T|^2 S_{\mathrm{eff}} = \frac{\omega^2 d_{\mathrm{eff}}^2 L_0^2 b_1^2}{2 S_{\mathrm{eff}} n_\omega^2 n_{2\omega} \varepsilon_0 c^3} P_1^2$. From Fig. 5, we can see that the intensity of the generated SH vector beams increases with the FF beams as a quadratic function. As shown in Fig. 5, when $P_1 = 350$ mW, the generated SH vector beams powers are 15.6 µW, 13.7 µW, and 12.2 µW, respectively, with topological charges $\ell = 1$, 2, and 3. That is because the divergence angle of the vortex beams relative to the center position becomes larger with the topological charge increasing, which leads to phase mismatching in the nonlinear frequency conversion process. Therefore, the intensity of the generated SH vector beams will decrease slightly. As for

the efficiency of generating SH vector beams, we consider $\ell = 1$ as an example, and we measure P_1 and P_2 corresponding to 350 mW and 15.6 µW, respectively. The normalized conversion efficiency of our method can be expressed as $\eta = \frac{P_2}{P_1^2 L_0^2} = \frac{\omega^2 d_{\mathrm{eff}}^2 b_1^2}{2 S_{\mathrm{eff}} n_\omega^2 n_{2\omega} \varepsilon_0 c^3}$. As a result, the conversion efficiency is about 5.09% W^{-1} cm^{-2}. The theoretical nonlinear efficiency of generating SH vector beams is 23.9% W^{-1} cm^{-2}. Because the first-order vortex beam diffracted by the fork grating has a small angle deflection relative to the incident FF beam, the phase-matching condition is not fully satisfied in the nonlinear frequency conversion process, resulting in a decrease of the efficiency of the nonlinear frequency conversion. To
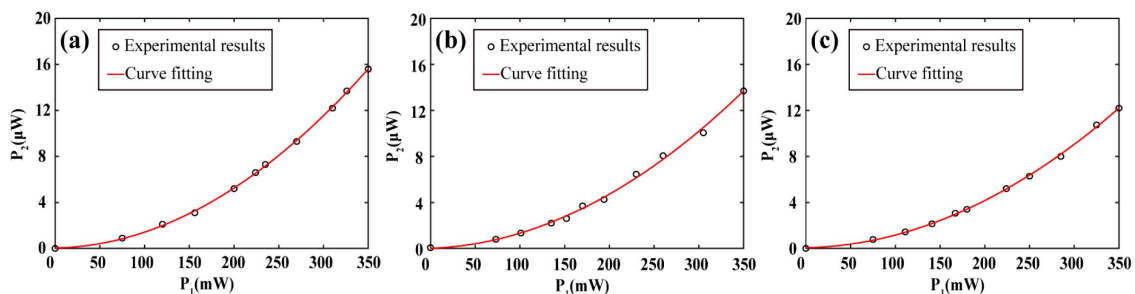

Fig. 5. Variation of generated SH vector beams power (P_2) as the incident FF beams power (P_1) increases before Sagnac loop. (a) $\ell = 1$, (b) $\ell = 2$, (c) $\ell = 3$.

generate vector beams with good quality, we make beams propagating clockwise and anticlockwise have the same intensity by changing the angle of the QWP_1, so that not all FF beams perform nonlinear frequency conversion, thus resulting in a decrease in nonlinear efficiency. The above two reasons are important factors that affect the nonlinear efficiency of generating SH vector beams. Furthermore, the inaccuracy of the temperature in the phase-matching process and cutting angle of the crystal in the experiment also result in the decrease of nonlinear conversion efficiency.

We propose a new way to generate vector beams of SH, which is more compact compared to the previous methods. In our experiments, only partial results are displayed, and we can obtain arbitrary linearly polarized vector beams by rotating the axis direction of the HWP_2 and changing the topological charge of the nonlinear fork grating. However, we find that with the increase of the topological charge, the intensity of generated SH vector beams decreases, as shown in Fig. 5. Therefore, the phase-matching angle bandwidth will be the limit or challenge to generate vector beams with large topological charge. In addition, we can generate more complex nonlinear vector optical fields such as multi-ring structures by designing microstructures purposefully. We employ LN crystal instead of an SLM, and thus our method can be used for high-power lasers. Also, for some frequency ranges that the SLM cannot modulate such as the ultraviolet waveband, it is an effective way to use microstructures of nonlinear crystal for phase modulation. In our experiment, the nonlinear conversion efficiency of generating vector beams of SH is much lower than the theoretical calculation, and we can achieve phase matching better by optimizing the crystal cutting angle and adjusting the temperature condition. Furthermore, our approach has potential use of vectorial fields in other nonlinear processes such as sum-frequency generation, difference-frequency generation, and optical parametric amplification. By choosing proper nonlinear crystals, it is possible to obtain vector beams with arbitrary wavelengths using such a nonlinear frequency conversion process, such as ultraviolet light and terahertz wave.

4. CONCLUSION

In conclusion, we have successfully realized the generation of nonlinear vectorial optical fields by using a compact nonlinear fork grating, which opens up new possibilities for all-optical switching and manipulation of vector beams. In our experiment, SH vector beams of different topological charges $\ell = 1, 2, 3$ are generated, and we analyze the vectorial properties by Stokes parameters theoretically and experimentally. Furthermore, arbitrary SH vector beams can be obtained by changing the axis direction of the HWP and the topological charge. Our approach may access vector beams at new wavelengths and find potential applications in optical micromanipulation, optical imaging, optical micromachining, classical and quantum optical communication, and so on.

REFERENCES

1. E. Snitzer, "Cylindrical dielectric waveguide modes," J. Opt. Soc. Am. **51**, 491–498 (1961).
2. T. Moser, H. Glur, V. Romano, *et al.*, "Polarization-selective grating mirrors used in the generation of radial polarization," Appl. Phys. B **80**, 707–713 (2005).
3. Y. Kozawa and S. Sato, "Generation of a radially polarized laser beam by use of a conical Brewster prism," Opt. Lett. **30**, 3063–3065 (2005).
4. X.-L. Wang, J. Ding, W.-J. Ni, *et al.*, "Generation of arbitrary vector beams with a spatial light modulator and a common path interferometric arrangement," Opt. Lett. **32**, 3549–3551 (2007).
5. P. Chen, W. Ji, B.-Y. Wei, *et al.*, "Generation of arbitrary vector beams with liquid crystal polarization converters and vector-photoaligned q-plates," Appl. Phys. Lett. **107**, 241102 (2015).
6. F. Yue, D. Wen, J. Xin, *et al.*, "Vector vortex beam generation with a single plasmonic metasurface," ACS Photonics **3**, 1558–1563 (2016).
7. S. Quabis, R. Dorn, M. Eberler, *et al.*, "Focusing light to a tighter spot," Opt. Commun. **179**, 1–7 (2000).
8. C. Min, Z. Shen, J. Shen, *et al.*, "Focused plasmonic trapping of metallic particles," Nat. Commun. **4**, 2891 (2013).
9. S. E. Skelton, M. Sergides, R. Saija, *et al.*, "Trapping volume control in optical tweezers using cylindrical vector beams," Opt. Lett. **38**, 28–30 (2013).
10. C. Hnatovsky, V. G. Shvedov, and W. Krolikowski, "The role of light-induced nanostructures in femtosecond laser micromachining with vector and scalar pulses," Opt. Express **21**, 12651–12656 (2013).
11. M. Meier, V. Romano, and T. Feurer, "Material processing with pulsed radially and azimuthally polarized laser radiation," Appl. Phys. A **86**, 329–334 (2007).
12. R. Chen, K. Agarwal, C. J. R. Sheppard, *et al.*, "Imaging using cylindrical vector beams in a high-numerical-aperture microscopy system," Opt. Lett. **38**, 3111–3114 (2013).
13. Z. Man, L. Du, C. Min, *et al.*, "Dynamic plasmonic beam shaping by vector beams with arbitrary locally linear polarization states," Appl. Phys. Lett. **105**, 011110 (2014).
14. W. Cheng, J. W. Haus, and Q. Zhan, "Propagation of scalar and vector vortex beams through turbulent atmosphere," Proc. SPIE **7200**, 720004 (2009).
15. Z. Zhu, M. Janasik, A. Fyffe, *et al.*, "Compensation-free high-dimensional free-space optical communication using turbulence-resilient vector beams," Nat. Commun. **12**, 1666 (2021).
16. H. Liu, H. Li, Y. Zheng, *et al.*, "Nonlinear frequency conversion and manipulation of vector beams," Opt. Lett. **43**, 5981–5984 (2018).
17. R. K. Saripalli, A. Ghosh, N. A. Chaitanya, *et al.*, "Frequency-conversion of vector vortex beams with space-variant polarization in single-pass geometry," Appl. Phys. Lett. **115**, 051101 (2019).
18. C. Yang, Z.-Y. Zhou, Y. Li, *et al.*, "Nonlinear frequency conversion and manipulation of vector beams in a Sagnac loop," Opt. Lett. **44**, 219–222 (2019).
19. Y.-C. Lou, Z.-M. Cheng, Z.-H. Liu, *et al.*, "Third-harmonic generation of spatially structured light in a quasi-periodically poled crystal," Optica **9**, 183–186 (2022).
20. H. Li, H. Liu, and X. Chen, "Nonlinear frequency conversion of vectorial optical fields with a Mach-Zehnder interferometer," Appl. Phys. Lett. **114**, 241901 (2019).
21. H. Li, H. Liu, and X. Chen, "Dual waveband generator of perfect vector beams," Photon. Res. **7**, 1340–1344 (2019).
22. H. Li, H. Liu, Y. Yang, *et al.*, "Ultraviolet waveband vector beams generation assisted by the nonlinear frequency conversion," Appl. Phys. Lett. **119**, 011104 (2021).
23. H. Li, H. Liu, Y. Yang, *et al.*, "Nonlinear generation of perfect vector beams in ultraviolet wavebands," Chin. Phys. Lett. **39**, 034201 (2022).

24. L. Zhang, F. Lin, X. Qiu, *et al.*, "Full vectorial feature of second-harmonic generation with full Poincaré beams," Chin. Opt. Lett. **17**, 091901 (2019).

25. L. Zhang, X. Qiu, F. Li, *et al.*, "Second harmonic generation with full Poincaré beams," Opt. Express **26**, 11678–11684 (2018).

26. S. Kumar, R. K. Saripalli, A. Ghosh, *et al.*, "Controlling the coverage of full Poincaré beams through second-harmonic generation," Phys. Rev. Appl. **19**, 034082 (2023).

27. N. Rubiano Da Silva, A. G. De Oliveira, M. F. Z. Arruda, *et al.*, "Stimulated parametric down-conversion with vector vortex beams," Phys. Rev. Appl. **15**, 024039 (2021).

28. H.-J. Wu, B. Zhao, C. Rosales-Guzmán, *et al.*, "Spatial-polarization-independent parametric up-conversion of vectorially structured light," Phys. Rev. Appl. **13**, 064041 (2020).

29. H.-J. Wu, B.-S. Yu, Z.-H. Zhu, *et al.*, "Conformal frequency conversion for arbitrary vectorial structured light," Optica **9**, 187–196 (2022).

30. Y. Yang, H. Li, H. Liu, *et al.*, "Highly efficient nonlinear vortex beam generation by using a compact nonlinear fork grating," Opt. Lett. **48**, 6376–6379 (2023).

31. H. Li, H. Liu, and X. Chen, "Nonlinear vortex beam array generation by spatially modulated fundamental wave," Opt. Express **25**, 28668–28673 (2017).